Load partition during hot deformation of AlSi12 and AlSi10Cu6Ni2 alloys: a quantitative evaluation of the stiffness of Si networks

David Canelo-Yubero[a,b,*]

Christoph Etzlstorfer[c]

Robert Koos[d]

Holger Germann[e]

Thomas Steffens[e]

Andreas Stark[f]

Elodie Boller[g]

Guillermo Requena[h,i]

[a] Nuclear Physics Institute ASCR, CZ-25068 Řež near Prague, Czech Republic

[b] Graz University of Technology, Institute of Materials Science, Joining and Forming, Kopernikusgasse 24/I, A-8010 Graz, Austria

[c] Voestalpine Stahl GmbH, Linz, Austria

[d] FRM II, TU München, Lichtenbergstraße 1, 85748 Garching, Germany

[e] KS Kolbenschmidt GmbH, Karl-Schmidt-Straße, 74172 Neckarsulm, Germany

[f] Helmholtz-Zentrum Geesthacht, Institute of Materials Research, Max-Planck-Str. 1, 21502 Geesthacht, Germany

[g] ESRF-The European Synchrotron, CS40220 Grenoble Cedex 9, France

[h] German Aerospace Center (DLR), Institute of Materials Science, Linder Höhe, D-51147 Cologne, Germany

[i] RWTH Aachen University, Metallic Structures and Materials Systems for Aerospace Engineering, Institute of Metal Forming, Intzestraße 10, D-52062 Aachen, Germany

*Corresponding Author: David Canelo-Yubero, Nuclear Physics Institute ASCR, CZ-25068 Řež near Prague, Czech Republic

ORCID id: 0000-0002-2423-4421

Email-address: caneloyubero@ujf.cas.cz

TE: +420 266 173 140

Fax: +420 220 940 141

Keywords: Synchrotron x-ray diffraction; Cast aluminium alloys; Hot deformation; Load partition; Synchrotron radiation computed tomography; Interconnectivity

Abstract

An eutectic AlSi12 alloy contains a rigid 3D network formed by the eutectic Si in the as-cast condition, which disintegrates during solution treatment. Synchrotron tomography proved that a near eutectic AlSi10Cu6Ni2 alloy also exhibits a 3D network with higher and more stable stiffness due to the presence of aluminides that retain the initial as-cast microstructure during the solubilization treatment and increase the volume fraction of rigid phases. In order to evaluate the load borne by different phases during hot deformation, in-situ synchrotron experiments were carried out revealing an underestimation of the load transfer from the soft

α-Al matrix to the hard silicon 3D network in the AlSi12 alloy. By taking into account the additional stiffness introduced by the local interconnectivity, the stresses in different phases in the near eutectic AlSi10Cu6Ni2 alloy were calculated. Additionally, the analysis of the aluminide Al_2Cu allowed to identify its influence in the global damage of the hybrid 3D network formed by the Si and aluminides in the near eutectic AlSi10Cu6Ni2 alloy.

1 Introduction

Aluminium-based alloys are extensively used in automotive and aeronautical industry. Among the cast aluminium alloys, the Al-Si system provides nearly 90% of all shape casting produced [1]. Typical automotive components are cylinder heads and pistons [1]. Slow solidification rate leads to the formation of eutectic Si plates embedded in the α-Al matrix (brittle behavior) while rapid cooling generate fibrous eutectic Si. The eutectic Si can present high interconnectivity, as showed by Bell et al. in the 1960s [2] by deep etching and verified more recently with 3-D techniques [3-4]. Solution heat treatments modify the morphological structure of the eutectic Si, a phenomenon called spheroidization [5]. This results in a loss of interconnectivity and the rounding of eutectic Si that yields a lower load carrying capability (e.g. [4] [4,6-7]). Morphology, distribution and interconnectivity of eutectic Si in Al-Si alloys vary their strength and ductility [4, 8-9]. The analysis of the load partition between the α-Al matrix and eutectic Si in a near eutectic cast AlSi alloy has already been reported for room temperature (RT) studies [4]. The 3D structure of eutectic Si in the as cast condition can be substantially modified by solution treatment, disintegrating the Si network into individual rounded and elongated particles.

Ni and Cu aluminides are rigid phases that increase the stiffness of the 3D Si network. Particularly, Ni-rich aluminides exhibit thermal stability at high temperature, becoming interesting for aluminium piston alloys. Some works [10-13] have initially proposed that a

relevant strengthening mechanism in Al-Si piston alloys at high temperature is given by the load carrying capability of the hybrid 3D interpenetrating multiphase networks of Si and aluminides. Furthermore, the disintegration and spheroidization during solution treatment of the eutectic 3D network of Si is highly supressed by the presence of these aluminides. First results showing quantitatively the load borne by these rigid phases in two different Al piston alloys have recently been presented in [14] and [15] for deformation tests performed at high and RT, respectively. The former inferred indirectly the stresses in the hybrid 3D network formed by the Si and aluminides while the second accounted independently for them in the sense that their mutual interactions as a consequence of the interconnectivity was not taken into account and led to an underestimation of their real load carrying capability.

Neutron and high energy synchrotron diffraction sources are bulk averaged diffraction techniques to evaluate in-situ the load transfer between different phases during deformation processes. When in-situ tests at high temperature are required, only synchrotron radiation produces short enough acquisition times to correctly track the physical processes avoiding relaxation mechanisms.

This work aims at evaluating the load partition among the α-Al matrix and the Si-phase in eutectic AlSi12 and near eutectic AlSi10Cu6Ni2 alloys during in-situ compression tests performed at high temperature. The stiffness of the 3D interpenetrating network of Si and Si-aluminides will be considered for a better understanding of the load partition between both types of phases. The volume fraction and connectivity of the Si-intermetallic network will be calculated by means of synchrotron tomographies.

2 Methodology

2.1 Materials

2.1.1 AlSi12 alloy

An eutectic AlSi12 alloy was produced by squeeze casting at Leichtmetallkompetenzzentrum Ranshofen (Austria) [16]. The chemical composition is shown in Table 1 [10]. The alloy was studied in as cast (AC) condition and after solution treatments (ST) at 500°C during 1 h and 4 h. All the samples in AC and ST condition were artificially overaged during 100 h at 300°C with subsequent air cooling to stabilize Si precipitates [17] .

The conventional metallography steps applied to different AlSi12 samples are detailed in [18].Fig. 1 shows light optical micrographs (LOM) of the AlSi12 alloy in different conditions, i.e. AC or 0 h ST, 1 h ST, and 4 h ST. The Si-phase in the AC condition exhibits a highly interconnected 3-D lamellar structure [4] although they are seen as needles in the 2D micrograph (Fig. 1 a). The α-Al matrix encloses the eutectic structure of the lamellar Si. The different ST times result in loss of the interconnectivity, showing isolated and rounded Si particles with the Al matrix surrounding the eutectic Si (Fig. 1b) and c)). These particles present short-fibre-like morphology [4].

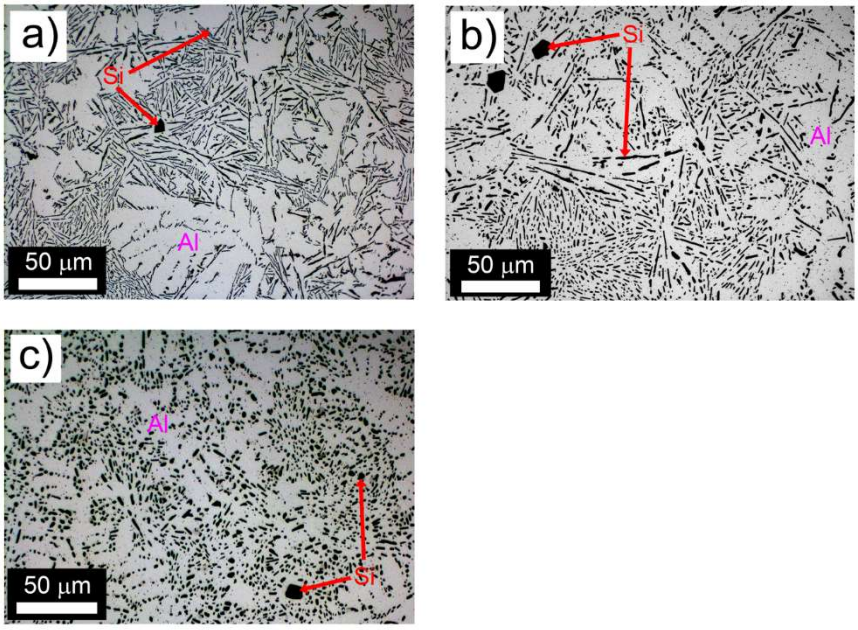

2.1.2 Aluminium piston alloy

A near eutectic AlSi10Cu6Ni2 piston alloy, hereafter 1062, was fabricated in the form of pistons by Kolbenschmidt [19] by gravity die casting [20]. Its chemical composition is shown in Table 2.

In addition to the AC condition, and identically to the AlSi12 alloy, ST of 1 h and 4 h at 500 °C were carried out with subsequent overageing (included the AC condition) at 300°C during 100 h to stabilize precipitates. The samples were cooled down in air. Fig. 2 a), b) and c) show light optical micrographs corresponding to the AC, 1 h and 4 h ST conditions, respectively. α-Al, primary and eutectic Si, and different aluminides [21] with irregular shape can be identified. Contiguity (shared interfaces) between Si and the different aluminides can be observed for all conditions. The AC platelet-like structure of Si is seen as needles in the 2D micrographs. The ST provokes a slight spheroidization of Si and aluminides, where platelet-like structures and coarse primary Si (Fig. 2 a)) become more rounded (Fig. 2 b) and c)).

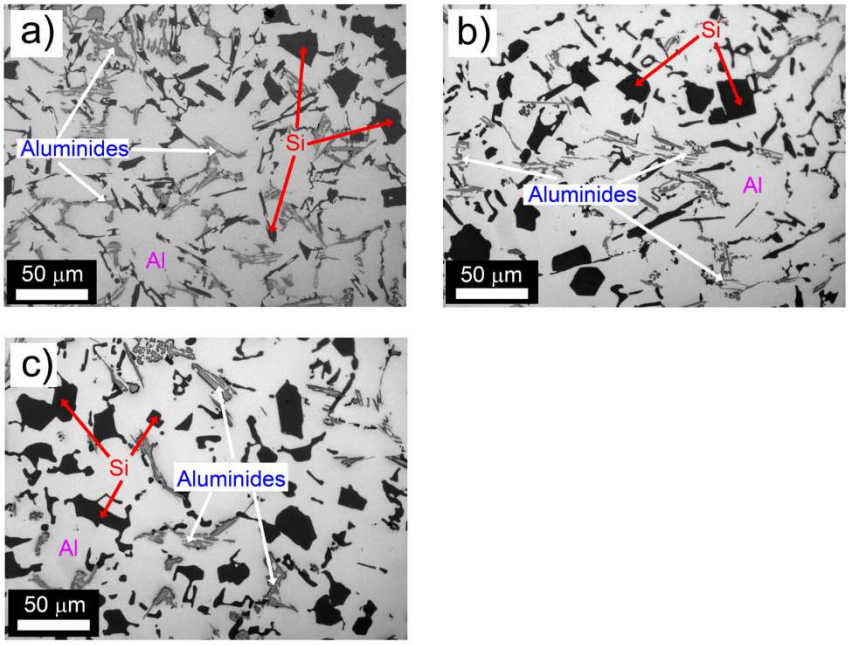

2.2 Synchrotron tomography

The 3D characterization of the 1062 alloy was performed at the ID19 beamline of the European Synchrotron Radiation Facility (ESRF) with a pink beam with maximum flux at 17.6 KeV and a FReLON camera [22]. The synchrotron x-ray computed tomography (sXCT) projections were recorded using an effective pixel size of $(0.28\ \mu m)^2$ and cylindrical samples with 0.6 mm diameter and 0.6 mm height were placed 39 mm behind the camera. 1000-1500 projections with exposure time of 0.1 s were used to scan a volume of ~ $420\times420\times500\mu m^3$ with a voxel size of $(0.28\mu m)^3$. Scans were reconstructed by applying a filtered backprojection algorithm that provided good confidence for the aluminides and low contrast of primary and eutectic Si with respect to the Al-matrix and consequently the use of a global threshold for image segmentation was hindered. Therefore, Si was segmented manually. Pre-processing and image processing were performed with Fiji/ImageJ software [23] and Avizo software [24].

2.3 Hot compression tests

In-situ angle dispersive high energy X-ray diffraction (HEXRD) experiments were performed in transmission mode during hot deformation at Harwi-II [25] at Doris III-Deutsches Elektronen-Synchrotron (DESY). The incident beam supplied an energy of 100 KeV (λ = 0.124 Å) with aperture slit dimensions of 1 × 1 mm^2. The acquisition time was set to 4s/frame and images collected using a 2-D (flat panel) MAR-555 detector with an array of 2560 (horizontal) × 3072 (vertical) pixels and pixel size of 139 × 139 μm^2. The sample-detector distance was set to 1534 mm and a capillary with LaB_6 powders was used to calibrate the distance and the instrumental broadening. Compression tests were carried out at a strain rate of 0.001 s^{-1} at 300°C in protective helium atmosphere with a Bähr dilatometer DIL 805 equipped with an induction heating coil system and a deformation unit. The synchrotron beam reached the 10 mm length and 5 mm diameter samples at 1.5 mm below a thermocouple spot-welded on its surface and at 3.5 mm from one side of the sample. A picture of the experimental setup at Harwi-II and a schematic lateral view are shown in Fig. 3 a) and b), respectively. A general schematic setup is also shown elsewhere [26]. After heating at 300 K/min, the samples were held during 1 min before the test started.

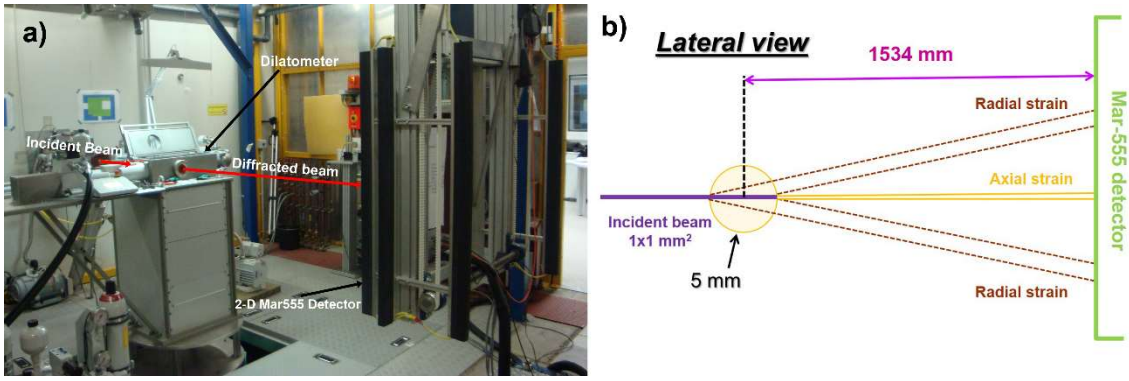

2.4 Strain and stress analysis

The phase strain evolution was evaluated considering the strain condition at the beginning of every compression test as reference. Two different strategies were used for the α-Al and Si phases on the one side and the aluminide Al_2Cu on the other side:

- α-Al and Si-phase: The 2D diffraction images were azimuthally integrated in cakes of 15° in both axial and radial directions using the software Maud [27,28] and least-squares Rietveld refinements were performed by considering only the α-Al and Si-phases although the former, owing to the poor statistics within the gauge volume as a result of the large grain size, did not show realistic strain evolution. Typical R_w (quality factor) values ranged from 5% to 15%.

-Al_2Cu: it was only possible to isolate one reflection of Al_2Cu-phase among different aluminides (intermetallic phases have in some cases low symmetry lattices leading to peak overlapping). The 2D diffraction images were also integrated in cakes of 15° in both axial and radial directions using the software Fit2D [29]. A Voigt function was used to fit the diffraction peak. This peak shift of the selected crystallographic plane *{hkl}* during deformation indicates a variation in the interplanar distance *d*.

The volume average strain calculation for both the Si and Al_2Cu-phases was determined as [30]:

$$\varepsilon_{i-Si} = \frac{a_i - a_0}{a_0} \qquad \text{Eq. (1)}$$

$$\varepsilon_{i-Al_2Cu} = \frac{d_i - d}{d} \qquad \text{Eq. (2)}$$

where ε_i is the strain at deformation step i, a_i/d_i and a_0/d_0 are the lattice parameters/interplanar distances for the deformation step i and the reference conditions, respectively, determined with the Bragg's law (for d_i and d_0) [31].

The evolution of principal stresses is calculated with the generalized Hooke's law:

$$\sigma_i = \frac{E}{1+\nu}\varepsilon_i + \frac{E\nu}{(1+\nu)(1-2\nu)}\left(\sum_{j=1}^{3}\varepsilon_j\right) \quad \text{Eq. (3)}$$

The principal stresses in the axial direction are indicated by σ_1, while those corresponding to the radial directions are σ_2 and σ_3. To simplify the calculations, a cylindrical symmetry is assumed, i.e., $\sigma_2 = \sigma_3$.

The Young's modulus E and the Poisson's ratio ν of the Si-phase were E_{Si} = 160 GPa and ν_{Si} = 0.22 [32].

3 Results

3.1 Microstructural characterization

Fig. 4 shows reconstructed sXCT volumes of the 1062 alloy after 0h (a and b), 1h (c and d), and 4h (e and f) ST at 500°C. The volume size is 56×56×56 μm^3 and Si (left side) and aluminide (right side) networks appear as blue and green, respectively. The Al matrix is transparent in these figures. Si-Aluminide interfaces are shown in grey in the volumes on the right side. Aluminides exhibit roughly constant volume fractions (8.3%-9.3%) and global interconnectivities (ratio between volume fraction of the largest particle of one phase with respect to the total volume fraction of the same phase [13]) after different ST as summarized in Table 3. The Si and the aluminides form an interconnected 3D network embedded in the α-Al matrix [10] that remains also practically constant in volume after the ST (21.4%-22%). Moreover, their interconnectivities, ranging from 98 to 99.7, are highly preserved because of their thermal stability (as demonstrated also in [13]).

Synchrotron tomographies have already been performed and reported in [4] for the AlSi12 alloy resulting in global interconnectivity of Si of ~ 100% for the AC condition, while a practically complete loss of connectivity (individual Si particles) are obtained after 4h of solution treatment.

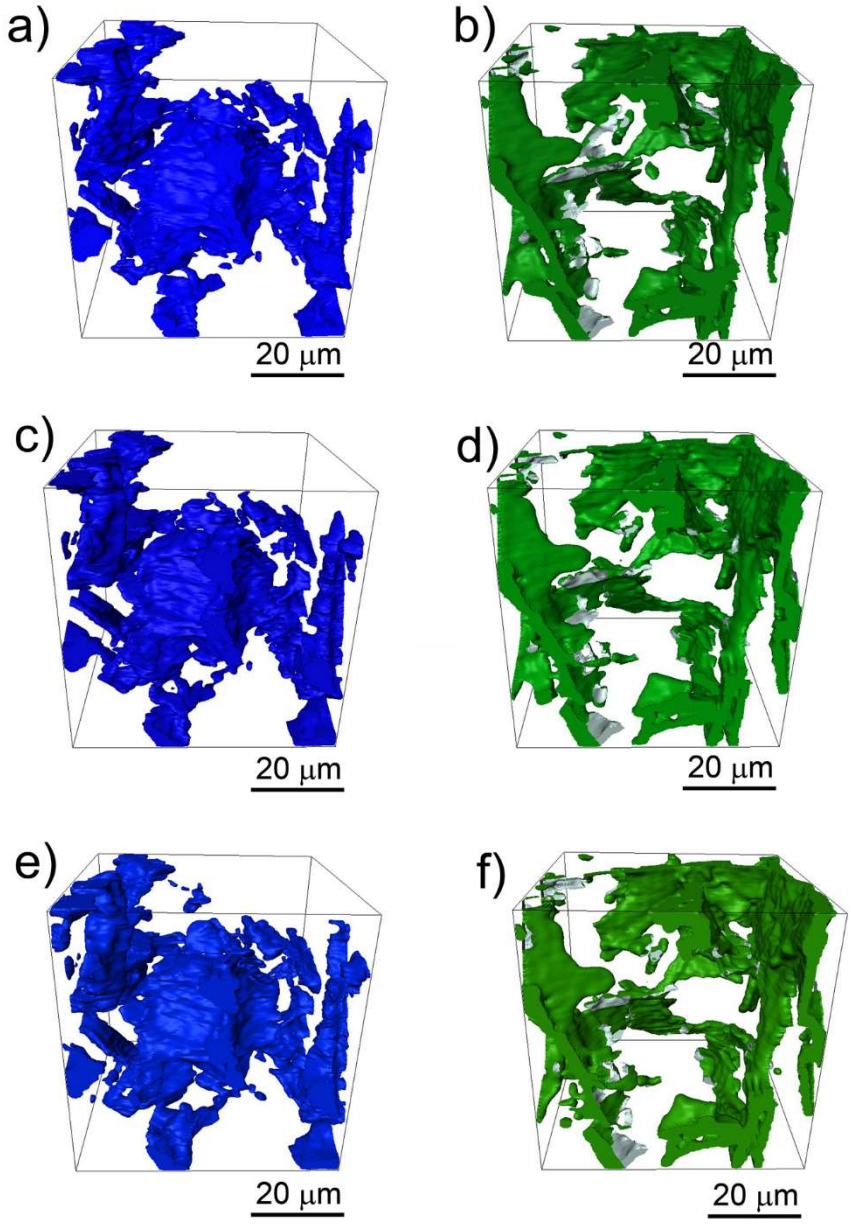

3.2 Macroscopic true stress-true strain curves

The resulting true-stress (calculated from the engineering stress and strain as $\sigma_{ts}=\sigma_{es}(1+\varepsilon_{es})$) vs. true-strain (calculated also from the engineering strain as $\varepsilon_{ts}=ln(1+\varepsilon_{es})$) curves for different ST conditions are shown for both alloys in Fig. 5. In case of the AlSi12 alloy, the

AC condition exhibits the highest strength with ~ 71 MPa and decreases to ~ 56 MPa by softening. The 1h and 4h conditions show maximum strengths of ~ 50 MPa and ~ 43 MPa, respectively. Both ST conditions slightly soften to ~ 44 MPa for the 1h ST and to ~ 40 MPa for the 4h ST.

For the 1062 alloy the AC condition exhibits also the highest strength, i.e. ~ 110 MPa with subsequent softening until a true strain of ~ 0.3, when the stress is similar to the to ST conditions. The 1h and 4 h ST conditions show a maximum strength of ~ 106 MPa, followed by softening down to ~ 75 MPa at the end of the test.

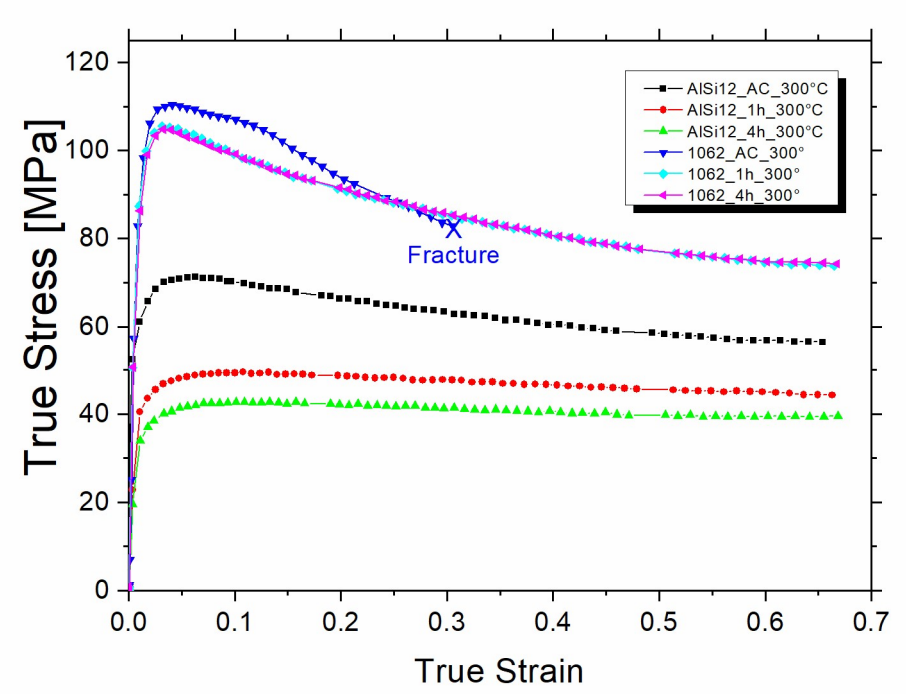

3.3 Crystallographic strains

3.3.1 AlSi12 alloy

Fig. 6 a shows the elastic lattice strain evolution for Si in AlSi12 upon different ST, i.e., AC, 1 h ST and 4 h ST. Typical error bars are given for each curve. The maximum axial strains observed are ~ - 1.6 × 10^{-3}, ~ - 1.1 × 10^{-3} and ~ - 0.9 × 10^{-3} for the AC condition, 1h and 4h ST, respectively. The radial direction strains reflect the Poisson's effect that result in positive

strain values. Subsequently, the axial strains evolve similarly to the macroscopic curves, with the highest softening in the AC condition, being similar for the 1h and 4h ST. Final strains are ~ - 1 × 10^{-3} for the AC and - 0.75 × 10^{-3} for the 1h and 4h conditions.

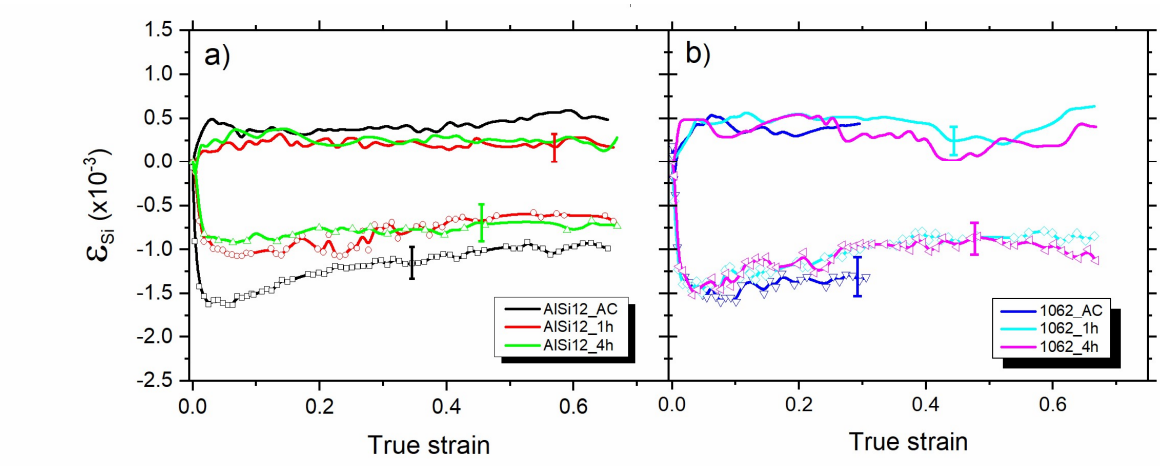

3.3.2 1062 piston alloy

The Si-phase (Fig. 6 b) for the AC condition has a maximum strain of ~ - 1.6 ~ 10^{-3} while for the ST conditions is ~ -1.5 ~ 10^{-3}, i.e., little differences are distinguishable. Subsequently, the strains decrease with similar softening slopes for all conditions, reaching at the end ~ -1 ~ 10^{-3} for the 1h and 4h ST. The radial direction strains reveal the Poisson's effect that results in positive or in some cases close to zero strains.

The lattice strain in the (110) crystallographic plane of the Al_2Cu phase (Fig. 7) develops maximum strains of ~ - 2 × 10^{-3}, ~ - 1.8 × 10^{-3} and ~ - 1.6 × 10^{-3} in the axial direction for the AC, 1h and 4h conditions, respectively. For the AC condition, the axial strain abruptly reduces to ~ - 1 × 10^{-3} at a true strain of ~ 0.04, remaining then practically constant, while for the 1h and 4h ST the strain drop occurs at a true strain of ~ 0.06 and of ~ 0.09 for the 4h and 1h ST, reaching subsequently a final strain of ~ -0.8. In the radial direction, the poor statistics hindered a reliable study of strain evolution. This is a consequence of the already commented

peak overlapping between different aluminides, and low total volume fraction of Al_2Cu phase (< 10 vol,%, see Table 3).

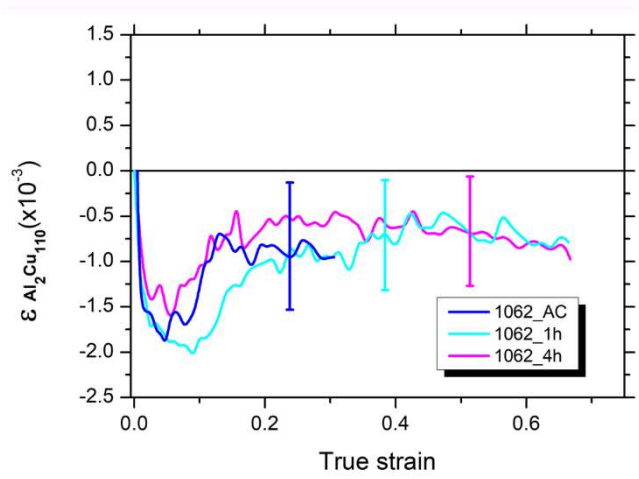

3.4 Load partition

3.4.1 Silicon

The load borne by the Si phase (calculated with Eq. (3)) is presented in Fig. 8 for the AlSi12 (left) and 1062 (right) alloys, respectively. The AC condition in both alloys together with the 1h condition of the 1062 alloy develop similar maximum stresses of ~ -250 MPa. The AlSi12 alloy evidences more differences for the 1h and 4h conditions, where the maximum stresses are ~ -175 MPa (1h) and ~ -140 MPa (4h). The 4h ST maximum stress for the 1062 alloy is slightly smaller than the AC and 1h conditions reaching ~ -250 MPa. All conditions for both alloys undergo softening resulting in a final stress of ~ -125 MPa at the end of the test. Similar stresses in the Si phase for both alloys in the AC condition evidence the primary role of the aluminides in load partition in the 1062 alloy.

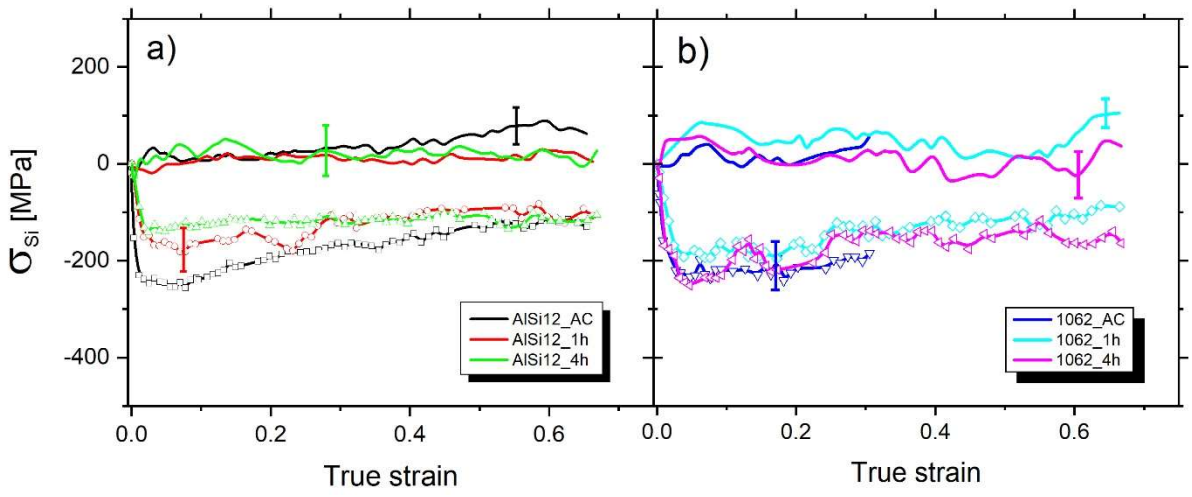

The volume fraction of Si corresponds to 13.5.% [4] and 12.1%-13.7% for the AlSi12 and 1062 alloys, respectively. This fact influences the calculated error bars in Fig. 8 and it consequently affects further calculations.

3.4.2 Aluminium

The α-Al stress evolution is only calculated for the AlSi12 alloy since the load borne by the intermetallics in the 1062 alloy is unknown due to the absence of interplanar strains for some of the aluminides. The rule of mixtures reads as:

$$\sigma_{applied} = (1 - f)\,\sigma_{\alpha-Al} + f \times \sigma_{Si} \qquad \text{Eq. (4)}$$

where $\sigma_{applied}$ is the macroscopic true stress, f is the Si volume fraction (13.5 vol.% from [4]), and $\sigma_{\alpha\text{-}Al}$ and σ_{Si} are the stresses in the α-Al and Si-phases, respectively. Therefore, $\sigma_{\alpha\text{-}Al}$ can be expressed as:

$$\sigma_{\alpha-Al} = \frac{\sigma_{applied} - f \times \sigma_{Si}}{(1-f)} \qquad \text{Eq. (5)}$$

Results are shown in Fig. 9. The maximum axial stress corresponds to the AC condition with ~ -45 MPa (ε ~ 0.04), remaining practically constant onwards. Maximum axial stresses for the 1h and 4h conditions at a true strain of ε ~ 0.01 are ~ -28 MPa and ~ - 24 MPa, respectively, with subsequent little variation to a final stress of ~ -30 MPa. Radial stresses are close to zero for all ST, reaching a maximum stress of ~ -10 MPa at the end of the AC test. This observation is contrary to the Poisson's effect and it could suggest that hydrostatic compressive stresses σ_H develop in the Al phase [15]. Hydrostatic stresses should be present in both phases to account for the strength differences. By observing Fig. 8, and assuming roughly that $\sigma_2 = \sigma_3 \sim 0$ MPa, yields $\sigma_H = (\sigma_1 + \sigma_2 + \sigma_3)/3 \sim \sigma_1/3$, which also confirms the presence of compressive σ_H in the Si-phase.

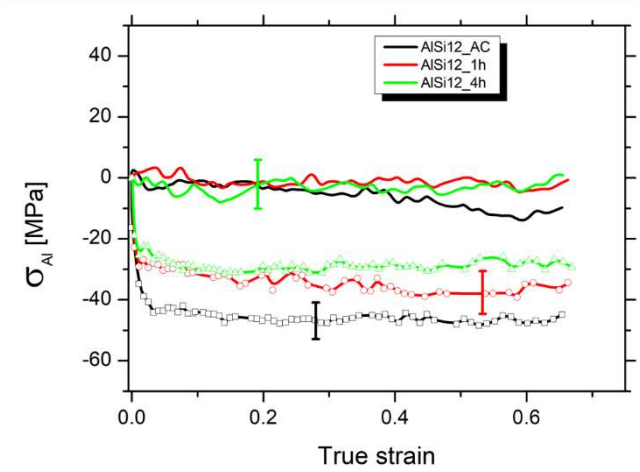

The α-Al matrix in the AlSi12 alloy has approx. 1.1 wt% of Si in solid solution at 540°C according to the Al-Si phase diagram [33,34]. Compression tests of an AlSi1.1 alloy (ST at 540°C) were performed at 300°C in [11] and the observed yield stress was -25 MPa, close to the 4h condition of the present work, in agreement with the present results. Nevertheless, similar maximum stresses could be expected in the α-Al matrix for the other AC and 1h conditions (but not higher) since matrices are the same.

4 Discussion

The stresses calculated for the α-Al phase in the AlSi12 alloy are indirectly based on those extracted from the Si-phase as stated in Eq. (5). The 3D network formed by the Si and its interconnecting branches, mainly in the AC condition, can be considered in a first approach as a cellular material. This type of structures can increase the stiffness of the solid material (e.g. [35]), i.e., the initially Young's modulus *E* considered for the Si-stress calculations is not valid for the highly 3D-interconnected network in the AC condition and, to a lesser extent, in the 1h condition (where the connectivity is not totally lost). This means that the calculations shown in the previous section (Fig. 8) are only valid when the initially interconnected network of Si totally disintegrates resulting in individual particles, i.e. for the α-Al and Si phases in the AlSi12 4h condition. Therefore, a different approach is needed to determine the stresses in the other two conditions. It is plausible to assume that the plastification behaviour expected for AlSi1.1 matrix should be rather similar for all ST conditions since 1) it plays a secondary role due to its low bearing capacity and 2) occurs during the early stages of deformation. In fact, when thermal mismatch occurs between the α-Al matrix and a second phase with a much lower coefficient of thermal expansion, as it is the case of Si, plastification should occur during heating before reaching 300°C [36] if relaxation mechanisms do not counteract this effect. Consequently, the α-Al stresses corresponding to the 4h ST will be used for the other two conditions of the AlSi12 alloy to recalculate *E* of the 3D Si network.

For the 1062 alloy, and due to the presence of Cu and Mg in the matrix that increases its yield strength by solid solution strengthening [15], different α-Al stresses are required to recalculate stresses of the 3D Si network (otherwise an artificial increase would be obtained). The yield strength of the matrix was already measured at 300°C for an alloy of similar composition to the one in this study [36], resulting in ~ -45 MPa. Comparing withFig. 8, it seems reasonable

to take the recalculated values for the α-Al in AlSi12 AC condition (Fig. 9) to estimate the stresses in the 1062 matrix as an approximation. This should represent a lower limit for this phase. Moreover, Chen et al [37] showed that in multi-component Al-Si-Cu-Ni-Mg-Fe alloys like the one studied in the present work all the aluminides exhibit roughly similar hardness up to 350°C. Therefore, the interconnected 3D hybrid network formed by Si and aluminides will be initially considered to be formed by one phase with uniform strength and elastic properties.

The recalculated stresses for the Si-phase in both AlSi12 and 1062 alloys are evaluated as follows (based on Eq. (4)):

$$\sigma_{Si-AlSi12} = \frac{\sigma_{applied} - (1-f) \times \sigma_{\alpha-Al\,4h}}{f} \quad \text{Eq. (6)}$$

$$\sigma_{Si+aluminides-1062} = \frac{\sigma_{applied} - (1-f') \times \sigma_{\alpha-Al\,AC}}{f'} \quad \text{Eq. (7)}$$

where $\sigma_{\alpha\text{-}Al\ 4h}$ and $\sigma_{\alpha\text{-}Al\ AC}$ is the load borne by the aluminium phase for the AlSi12 alloy in the 4h and AC conditions, respectively, f the Si vol.% for the AlSi12 (13.5% [4]), and f' the Si + aluminide network vol.% for the 1062 (21.4, 21.4 and 22.0 for the 0h, 1h and 4h conditions from Table 3).

The results are presented in Fig. 10 for the AlSi12 (left) and 1062 (right) alloys, respectively. Compared toFig. 8, there is a noticeable increase in the load borne by the Si-phase (except for the AlSi12 4h condition that remains equal) after accounting for its real stiffness. For the AlSi12 alloy, the highest stress is ~ -350 MPa (AC) while for the 1h condition is ~ -200 MPa. Analyzing the 1062 alloy, the stress increment in the Si + aluminides network is similar to that of the AlSi12 alloy in AC condition, i.e., from ~ -360 MPa (AC) to ~ -340 MPa (4h ST). These curves evolve identically to the macroscopic stresses exhibiting further softening.

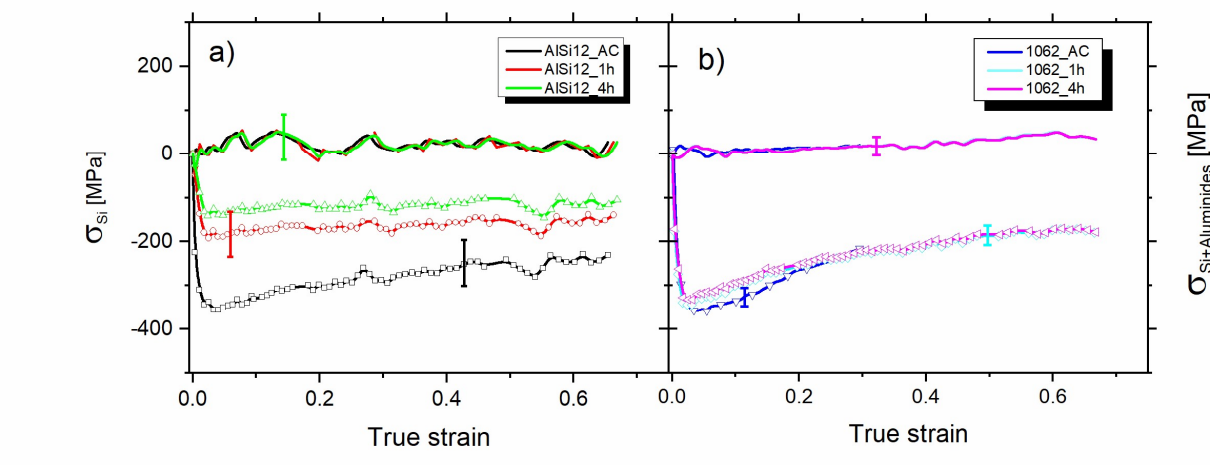

The load transfer Al-to-Si can be described to some extent. During loading of the AlSi12 alloy, axial stresses in the Si-phase increase as a function of the applied strain with different slopes depending on the ST time. Thus, the AC condition (i.e. 0h ST) shows a steeper stress increase than the other ST conditions for the same applied strain. This indicates that the Si network in the AC condition is able to carry a larger load portion than 1h and 4h ST for identical externally applied strains owing to its higher stiffness. This more effective load transfer from the α-Al matrix to the 3D Si network in AC condition was proposed in [11] and [13] for compression tests at 300°C for AlSi12 and AlSi10Cu5Ni2 alloys, respectively. There, the decrease in the stress carried by the Si after solution treatments was attributed to the spheroidization of the 3D Si network, which is a combined process of disintegration of 3D networks of Si and further rounding of the disconnected particles. This effect is very pronounced for the AlSi12 alloy [12].

The maximum stress difference of the hybrid 3D network between the 0 h and 4h conditions of the 1062 alloy (Fig. 10) is ~ 20 MPa, much smaller than for the AlSi12 alloy since the global interconnectivity of Si is highly preserved even after 4h ST [13]. Macroscopically, the higher strength observed for the 1062 alloy in AC condition when compared to the 1h and 4h STs can be ascribed to the local connectivity loss (i.e., a lower number of branches forming

the 3D interconnected network) between the Si and the Cu-rich aluminides as already stated in [38] (the global connectivity is preserved). Moreover, the 1062 alloy shows, in all conditions, a similar and effective load transfer from the α-Al matrix to the Si 3D network when compared to the AlSi12 alloy in AC condition reflected by similar stress increase.

The damage mechanisms in an AlSi10Cu5Ni2 alloy have already been analysed by Asghar et al. [39], namely fracture of aluminides and Si (primary and eutectic) together with debonding between α-Al matrix and Si/aluminides. Additionally, voids tend to be oriented preferentially in the load direction.

The addition of Ni, even in small amounts of 1 wt.%, increase the thermal stability by the formation of highly interconnected thermal aluminides [11], while the presence of Cu contributes to the formation of alumnides that increase their interconnectivity [13]. Al_2Cu is one of the phases forming the hybrid 3D structure of aluminides and Si [10,21]. Its contribution to strengthen the alloy is reflected by the strain slopes for all conditions in axial direction (Fig. 7). In spite of the large error bars in Fig. 7, which hinder a more precise analysis, it is reasonable to assume that this phase fails within the true strain interval [0.05-0.1]. Asghar et al. [39] reported that fracture of aluminides during compression tests at 300°C of the AlSi10Cu5Ni2 alloy takes place at $\varepsilon \sim 0.04$, which is practically the lower limit of the commented interval.

The results obtained in this work for the 1062 alloy show that the maximum stresses in the Si 3D network occur at the same time or later than the strain drop in the Al_2Cu phase takes place, suggesting that the Al_2Cu phase plays a relevant role controlling the global failure of the 3D network or at least is one of the first aluminides to fail. The presence of Ni within its structure, providing thermal stability, cannot be disregarded although in this work was not possible to resolve it.

The generalized Hooke's law (see Eq.(3)) can be also be written for the axial and radial strains as follows:

$$\varepsilon_1 = \frac{1}{E}[\sigma_1 - \nu(\sigma_2 + \sigma_3)] \quad \text{Eq. (8)}$$

$$\varepsilon_3 = \frac{1}{E}[\sigma_3 - \nu(\sigma_1 + \sigma_2)] \quad \text{Eq. (9)}$$

where ε_i, σ_i, E and ν have their common meanings. From Eq.(9), equalling σ_2 and σ_3, yields:

$$\varepsilon_3 \times E = \sigma_3 - \nu(\sigma_1 + \sigma_3) \rightarrow \nu = \frac{\sigma_3 - \varepsilon_3 \times E}{\sigma_1 + \sigma_3} \quad \text{Eq. (10)}$$

Eq. (10) can be substituted in Eq. (8) yielding:

$$\varepsilon_1 \times E = \sigma_1 - 2 \times [\frac{\sigma_3 - \varepsilon_3 \times E}{\sigma_1 + \sigma_3}] \times \sigma_3$$

And E can be expressed as follows:

$$E = \frac{(\sigma_1 - \frac{2 \times \sigma_3^2}{\sigma_1 + \sigma_3})}{(\varepsilon_1 - \frac{2\varepsilon_3 \times \sigma_3}{\sigma_1 + \sigma_3})} \quad \text{Eq. (11)}$$

The recalculated E for the 3D Si and 3D Si + aluminide networks of the AlSi12 and 1062 alloys, respectively, is shown in Fig. 11. For the AlSi12, the stiffness is increased by 25% and 50% for the 1h and AC conditions, respectively. The presence of the aluminides in the 1062 alloy retain the stiffness of the Si network in all conditions and shows its efficiency with similar stiffness than the AlSi12 alloy in AC condition. This finding validates the assumption of considering the 3D Si + aluminide network as a unique phase due to its solidary behaviour with uniform strength and elastic properties. These 3D Si+ aluminide E modules can be used for experiments performed at lower temperatures and with a simple analysis of the Si-phase strains can be sufficient not only to deduce the stresses in the rigid 3D Si network but also in α-Al matrix.

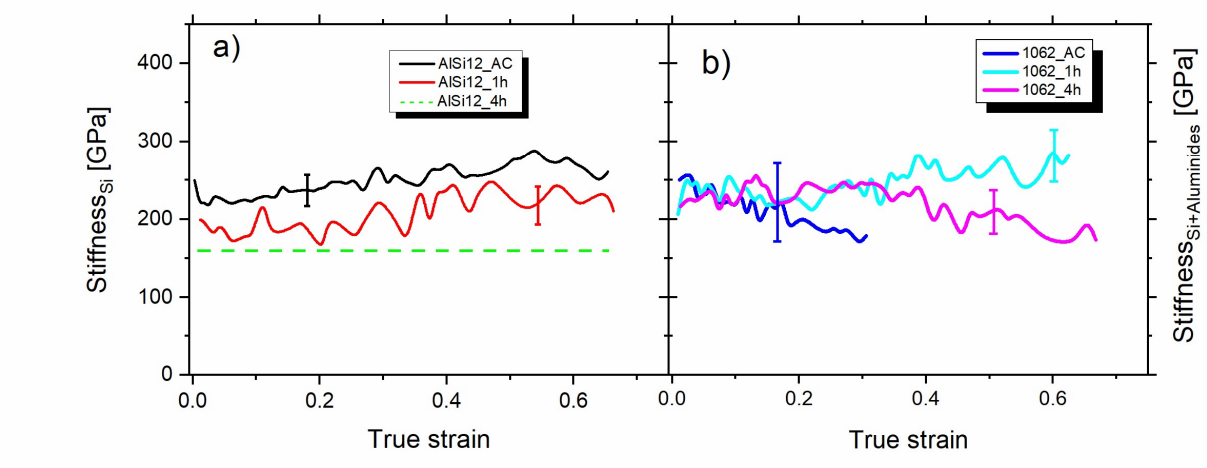

Non negligible error bars are distinguishable in Fig. 11 for the stiffness, mainly for the 1062 alloy in AC condition. Since they are based on those observed in Fig. 10, it is possible to obtain an estimation of their influence on the true stress-true strain curves. Typical errors of ~ ±50 MPa and ~ ±25 MPa are distinguishable for the AlSi12 and 1062 alloys, respectively (Fig. 10). Applying the rule of mixtures, the former should be affected by 0.135 [4] and the second by ~ 0.22 (Table 3), yielding maximum errors of ~ ±7 MPa and ~ ±6 MPa, respectively. These errors, except for the AlSi12 ST conditions (where the connectivity is practically lost), represent ≤ 12% of total macrostresses-strain curves (Fig.5), i.e. a reasonably low influence, and it is used to confirm the relatively good accuracy of the present work.

5 Conclusions

In-situ compression tests were carried out during high energy X-ray diffraction for a eutectic AlSi12 alloy and a near eutectic AlSi10Cu6Ni2 alloy. Additionally, synchrotron x-ray computed tomography was performed only in the near eutectic AlSi10Cu6Ni2 alloy. The following conclusions can be drawn from this work:

- The near eutectic AlSi10Cu6Ni2 alloys exhibits a 3D highly interconnected network formed by the Si and aluminides embedded in the α-Al matrix.

- The eutectic 3D Si network in the near eutectic AlSi10Cu6Ni2 alloys is capable of bearing a higher load than in the eutectic AlSi12 alloy in corresponding heat treatment conditions (except for the AC condition that is similar) owing to the presence of highly interconnected 3D networks of aluminides. These aluminides partially avoid the spheroidization of eutectic Si during the solution treatments conserving thus its load bearing capability.
- Aluminides play a primary role in the load bearing capability in the near eutectic AlSi10Cu6Ni2 alloy by 1) increasing the volume fraction of the rigid phases and 2) producing a hybrid 3D Si + intermetallic network with similar stiffness to the 3D Si network of the AlSi12 alloy in AC condition.
- The Al_2Cu-phase, which can also include Ni within its structure, plays an important role on the onset of the damage in the near eutectic AlSi10Cu6Ni2 alloy since it seems to be one of the first aluminides to fracture of the 3D hybrid network formed by the Si and intermetallic phases during the high temperature compression tests.
- The stiffness of the silicon network by considering the connectivity of different phases was calculated and resulted, compared to isolated Si particles, in an increase of ~ 25% and ~ 50% for the 1h and 4h solution treatment conditions of the eutectic AlSi12 alloy and of ~ 50% for the near eutectic AlSi10Cu6Ni2 alloy in all conditions.

6 Acknowledgements

The financial support from the FWF (Austrian Science Fund) project P22876-N22 is acknowledged. David Canelo-Yubero would also like to thank the partial financial support from the FWF projects P27471-N19 and P29727. The authors would like to thank the allocation of beamline at Harwi-II (DESY) in the framework of proposal I-20160441 EC and

at the ESRF in the frame of proposal IN662. Authors thank T. Lippmann (Helmholz-Zentrum Geesthacht) for the support during beamtime.

Conflicts of interest

The authors declare that they have no conflict of interest.

[1] Davis JR (Ed.) (1993) ASM specialty handbook: Aluminium and Aluminium alloys, Ohio.
[2] Bell JAE, Winegard WC (1965) Interconnexion of silicon in modified aluminium-silicon eutectic, Nature 208: 177.
[3] Lasagni F, Lasagni A, Marks E, Holzapfel C, Mücklich F, Degischer HP (2007) Three dimensional characterization of 'as-cast' and solution-treated AlSi12(Sr) alloys by high-resolution FIB tomography, Acta Mater 55:3875-3882.
[4] Requena G, Garces G, Rodríguez M, Pirling T, Cloetens P (2009) 3D architecture and load partition in eutectic Al-Si alloys, Adv Eng Mater 11:1007-1014.
[5] Zhu PY, Liu QY, Hou TX (1985) Spheroidization of eutectic silicon in Al-Si alloys, AFS transactions 93:609-614.
[6] Requena G, Garcés G, Danko S, Pirling T, Boller E (2009) The effect of eutectic Si on the strength of short-fibre-reinforced Al, Acta Mater 57:3199-3210.
[7] Winand HMA, Whitehouse AF, Withers PJ (2000) An investigation of the isothermal creep response of Al-based composites by neutron diffraction, Mater Sci Eng A 284:103-113.
[8] Sahoo M, Smith RW (1975) Mechanical properties of unidirectionally solidified Al-Si eutectic alloys, Met Sci 9:217-222.
[9] Hosch T, Napolitano RE (2010) The effect of the flake to fiber transition in silicon morphology on the tensile properties of Al-Si eutectic alloys, Mater Sci Eng A 528:226-232.
[10] Asghar Z, Requena G, Degischer HP, Cloetens P (2009) Three-dimensional study of Ni aluminides in an AlSi12 alloy by means of light optical and synchrotron microtomography, Acta Mater 57:4125-4132.
[11] Asghar Z, Requena G, Kubel F (2010) The role of Ni and Fe aluminides on the elevated temperature strength of an AlSi12 alloy, Mater Sci Eng A 527:5691-5698.
[12] Asghar Z, Requena G, Boller E (2010) 3D interpenetrating hybrid network of rigid phases in an AlSi10Cu5NiFe piston alloy, Prakt Metallogr 47:471-486.
[13] Asghar Z, Requena G, Boller E (2011) Three-dimensional rigid multiphase networks providing high-temperature strength to cast AlSi10Cu5Ni1-2 piston alloys, Acta Mater 59:6420-6432.
[14] Bugelnig K, Germann H, Steffens T, Sket F, Adrien J, Maire E, Boller E, Requena G (2018) Revealing the effect of local connectivity of rigid phases during deformation at high temperature of cast AlSi12Cu4Ni(2,3)Mg alloys, Materials 11:1300.
[15] Evsevleev S, Mishurova T, Cabeza S, Koos R, Sevostianov I, Garcés G, Requena G, Fernández R, Bruno G (2018) The role of intermetallics in stress partitioning and damage evolution of AlSi12CuMgNi alloy, Mater Sci Eng A 736:453-464.
[16] http://www.lkr.at/
[17] Lasagni F, Mingler B, Dumont M, Degischer HP (2008) Precipitation kinetics of Si in aluminium alloys, Mater Sci Eng A 480:383-391.
[18] Lasagni FA (2006) The role of Si on the microstructure of Al casting alloys and short fibre composites, PhD thesis, Vienna University of Technology.
[19] http://www.kspg.com/
[20] Polmear IJ (2006) Light Alloys, Elsevier, Butterworth-Heinemann, Oxford.
[21] Koos R (2014) Correlation between 3D microstructure and thermo-mechanical behavior of near eutectic piston alloys, PhD-Thesis, TU-Vienna.
[22] Labiche JC, Mathon O, Pascarelli S, Newton MA, Ferre GG, Curfs C, Vaughan G, Homs A, Fernandez Carreiras D (2007) The fast readout low noise camera as a versatile x-ray detector for time resolved dispersive

extended x-ray absorption fine structure and diffraction studies of dynamic problems in materials science, chemistry, and catalysis, Rev Sci Instrum 78:1-11.
[23] http:/rsbweb.nih.gov/ij/
[24] AvizoFire http://www.vsg3d.com/
[25] Beckmann F, Dose T, Lippmann T, Lottermoser L, Martins RV, Schreyer A (2007) The new materials science beamline HARWI-II at DESY, AIP Conf Proc 879:746-749.
[26] Canelo-Yubero D, Requena G, Sket F, Poletti C, Warchomicka F, Daniels J, Schell N, Stark A (2016) Load partition and microstructural evolution during in situ hot deformation of Ti-6Al-6V-2Sn alloys, Mater Sci Eng A 657:244-258.
[27] Lutterotti L, Matthies S, Wenk HR, Schultz AS, Richardson JW (1997) Combined texture and structure analysis of deformed limestone from time-of-flight neutron diffraction spectra, J Appl Phys 81:594-600.
[28] Lutterotti L, Bortolotti M, Ischia G, Lonardelli I, Wenk HR (2007) Rietveld texture analysis from diffraction images, Z Kristallogr Suppl 26:125-130.
[29] Hammersley AP, Svensson SO, Hanfland M, Fitch AN, Häusermann D (1996) Two-dimensional detector software: from real detector to idealized image of two-theta scan, High Press Res 14:235-248.
[30] Reimers W (2008) Introduction to diffraction methods for internal stress analyses. In: Reimers W, Pyzalla AR, Schreyer A, Clemens H (Eds) Neutrons and Synchrotron Radiation in Engineering Materials Science, Wiley-VCH, Weinheim, pp 115-135.
[31] Lodini A (2003) Calculation of residual stress form measured strain. In: Fitzpatrick ME, Lodini A (Eds) Analysis of Residual Stress by Diffraction using Neutron and Synchrotron Radiation, Taylor&Francis, London, pp 47-59.
[32] Huber T, Degischer HP, Lefranc G, Schmitt T (2006) Thermal expansion studies on aluminium-matrix composites with different reinforcement architecture of SiC particles, Compos Sci Technol 66:2206-2217.
[33] Massalski TB (1986) Binary Alloy Phase Diagrams, vol. 1, ASM, Metals Park, Ohio.
[34] Murray JL, McAlsiter AJ (1984) Bulletin of Alloy Phase Diagrams 5:74-84.
[35] Evans AG, Hutchinson JW, Ashby MF (1998) Curr Opin Solid St M 3:288-303.
[36] Requena G, Canelo Yubero D, Corrochano J, Repper J, Garcés G (2012) Stress relaxation during thermal cycling of particle reinforced aluminium matrix composites, Compos Part A-Appl S 43:1981-1988.
[37] Chen CL, Richter A, Thomson RC (2010) Investigation of mechanical properties of intermetallic phases in multi-component Al/Si alloys using hot-stage nanoindentation, Intermetallics 18:499-508.
[38] Bugelnig K, Sket F, Germann H, Steffens T, Koos R, Wilde F, Boller E, Requena G (2018) Influence of 3D connectivity of rigid phases on damage evolution during tensile deformation of an AlSi12Cu4Ni2 piston alloy, Mater Sci Eng A 709:193-202.
[39] Asghar Z, Requena G (2014) Three dimensional post-mortem study of damage after compression of cast Al-Si alloys, Mater Sci Eng A 591:136-143.

Figure captions

Fig. 1 Light optical micrographs of the AlSi12 alloy showing the α-Al, and eutectic Si and primary Si in a) AC condition, b) 1 h ST and c) 4 h ST

Fig. 2 Light optical micrographs of the 1062 piston alloy showing the α-Al, eutectic Si and primary Si, and aluminides in a) AC condition, b) 1 h ST and c) 4 h ST.

Fig. 3 a) Picture of the experimental setup at Harwi-II at DESY. b) Schematic lateral view of the setup

Fig. 4 3D reconstructed volumes of the Si (blue) and aluminides (green) networks after solution treatments at 500°C during a) and b) 0h, c) and d) 1h, and e) and f) 4h

Fig. 5 True stress vs. true strain curves obtained during compression tests at 300°C for the AlSi12 and 1062 alloys with different solution treatment times at 500°C

Fig. 6 Lattice strain evolution during compression tests at 300°C for the Si phase in the axial (open symbols) and radial directions (full lines) for the a) AlSi12 and b) 1062 alloys. Typical error bars are indicated

Fig. 7 Interplanar strain evolution during compression tests at 300°C for the Al_2Cu-phase of the 1062 piston alloy in axial direction. Typical error bars are indicated

Fig. 8 Evolution of the load borne by Si-phase during compression tests at 300°C in axial (open symbols) and radial (full lines) directions for the a) AlSi12 and b) 1062 alloys. Typical error bars are indicated

Fig. 9 α-Al stress evolution during compression tests at 300°C in the axial (open symbols) and radial (full lines) directions for the AlSi12 alloy. Typical error bars are indicated

Fig. 10 Recalculated stress evolution during compression tests at 300°C in axial (open symbols) and radial (full lines) directions for the a) 3D Si and b) 3D Si + aluminide networks in AlSi12 and 1062 alloys, respectively. Typical error bars are indicated

Fig. 11 Calculated stiffness for the a) 3D Si and b) 3D Si+Aluminide networks during compression tests at 300°C in AlSi12 and 1062 alloys, respectively. Typical error bars are indicated